Bursting and critical layer frequencies in minimal turbulent dynamics and connections to exact coherent states

Jae Sung Park
Department of Mechanical and Materials Engineering, University of Nebraska–Lincoln, Lincoln, Nebraska 68588-0526, USA

Ashwin Shekar and Michael D. Graham*
Department of Chemical and Biological Engineering, University of Wisconsin–Madison, Madison, Wisconsin 53706-1691, USA

(Received 29 August 2016; published 25 January 2018)

The dynamics of the turbulent near-wall region is known to be dominated by coherent structures. These near-wall coherent structures are observed to burst in a very intermittent fashion, exporting turbulent kinetic energy to the rest of the flow. In addition, they are closely related to invariant solutions known as exact coherent states (ECS), some of which display nonlinear critical layer dynamics (motions that are highly localized around the surface on which the streamwise velocity matches the wave speed of ECS). The present work aims to investigate temporal coherence in minimal channel flow relevant to turbulent bursting and critical layer dynamics and its connection to the instability of ECS. It is seen that the minimal channel turbulence displays frequencies very close to those displayed by an ECS family recently identified in the channel flow geometry. The frequencies of these ECS are determined by critical layer structures and thus might be described as "critical layer frequencies." While the bursting frequency is predominant near the wall, the ECS frequencies (critical layer frequencies) become predominant over the bursting frequency at larger distances from the wall, and increasingly so as Reynolds number increases. Turbulent bursts are classified into strong and relatively weak classes with respect to an intermittent approach to a lower branch ECS. This temporally intermittent approach is closely related to an intermittent low drag event, called hibernating turbulence, found in minimal and large domains. The relationship between the strong burst and the instability of the lower branch ECS is further discussed in state space. The state-space dynamics of strong bursts is very similar to that of the unstable manifolds of the lower branch ECS. In particular, strong bursting processes are always preceded by hibernation events. This precursor dynamics to strong turbulence may aid in development of more effective control schemes by a way of anticipating dynamics such as intermittent hibernating dynamics.

DOI: 10.1103/PhysRevFluids.3.014611

I. INTRODUCTION

In the near-wall region of wall-bounded shear flows, turbulent flows are known to be dominated by coherent structures comprised of quasistreamwise vortices staggered in the flow direction [1]. These near-wall coherent structures are self-sustained, exporting turbulent kinetic energy to the rest of the flow [2]. The production of turbulent kinetic energy is observed to occur quasi-periodically over time [1,3–6]. This temporally intermittent turbulent phenomenon called a burst is responsible for virtually

*Corresponding author: mdgraham@wisc.edu

all of the production of turbulent kinetic energy in the near-wall region. Thus, the bursting frequency is an important characteristic of turbulent flows, which is present at all distances from the wall and in all canonical wall-bounded turbulent flows [7].

The term "burst" was coined by Kline *et al.* [8] to describe the abrupt breakup process of low-speed streaks occurring on a very short time scale. Since then, substantially more has been learned about the bursting process with the help of the advances in experimental techniques [9–11] and numerical simulation capabilities [12,13], and many studies suggest connections between the bursting process and coherent structures in turbulent flow [1,14]. A comprehensive summary of progress on the understanding of the bursting process is provided by Jiménez [7]. In particular, this work presented a detailed discussion on bursting in the buffer layer, which is related to the present work. More recently, Jiménez [4,15] used the Orr mechanism arising in the linearized Navier-Stokes (Orr-Sommerfeld) equation to describe a burst as a linear process in minimal channel. It is shown that the evolution of a burst in a fully nonlinear turbulent flow in a minimal channel can be well described by the Orr-like transient amplification of disturbances over times of the order of 15% of an eddy turnover time. Adrian [16] provided evidence that turbulent bursts coincide with coherent structures such as hairpin vortices. The connection between a turbulent burst and near-wall coherent structures is the focus of the present work.

The study of near-wall coherent structures has been greatly advanced by the discovery of exact coherent states (ECS) [17,18]. These states are nontrivial invariant solutions to the Navier-Stokes equations, some of which take the form of nonlinear traveling waves (TW)– steady states in a reference frame translating at a constant streamwise speed. The TW solutions have enabled *a priori* study of self-sustained near-wall coherent structures that resemble in many ways that transient structures observed in fully turbulent flows [19]. In addition to TW solutions, other types of ECSs are equilibria and periodic or relative periodic orbits [20]. These invariant solutions to the governing equations have been found numerically in all canonical wall-bounded geometries for turbulent flows (plane Couette and Poiseuille, pipe and boundary layer) [18,20–31]. In general, these solutions have a spatial structure in the form of low-speed streaks that are wavy in the streamwise direction, straddled by counter-rotating streamwise-aligned vortices; that is, they have the same basic qualitative structure as near-wall turbulence. The basic self-sustaining process underlying these structures has been qualitatively described by Waleffe [32].

Exact coherent states primarily arise in pairs at a so-called "saddle-node" bifurcation point at a particular Reynolds number (Re). At such a bifurcation, the pair of solutions emerges at finite amplitude; we refer to each pair of solutions as a solution family. Away from such bifurcation point, the difference of the amplitude between the solutions grows as Re increases. In general, the upper-branch (UB) solution of each pair has a large velocity fluctuation at a given Re, denoted as a high drag state, compared with its corresponding lower-branch (LB) solution.

Exact coherent states have been shown to be closely related to the bursting phenomenon [5,33–37]. For channel flow, Itano and Toh [33] linked the bursting process to an instability of the traveling wave solution, suggesting that the bursting process is a shadow of a traveling wave solution and its unstable manifolds. They also used periodic-like solutions with which the recursive nature of the bursting process is explained qualitatively [35]. For Couette flow, the bursting phenomenon was explained in terms of periodic and relative periodic solutions to the Navier-Stokes equations [34,37]. Kawahara and Kida [34] suggested that heteroclinic connections between two periodic solutions may serve as the paths of the bursting trajectories because heteroclinic events appear to capture key features of the bursting process. Because of the clear connection between the bursting phenomenon and the instability of exact coherent states, the present work focuses on the relationship between the bursting processes and the unstable manifolds of the TW solutions recently identified by Park and Graham [38], which will be presented in Sec. III D.

In related work, substantial intermittency between high and low drag states has been found by using direct numerical simulations (DNS) at low Reynolds numbers in the minimal channel flow geometry. Particularly relevant in this regard is the study by Xi and Graham [39,40]. These authors showed that a minimal channel flow cycles intermittently between "active" intervals, with high drag characteristics

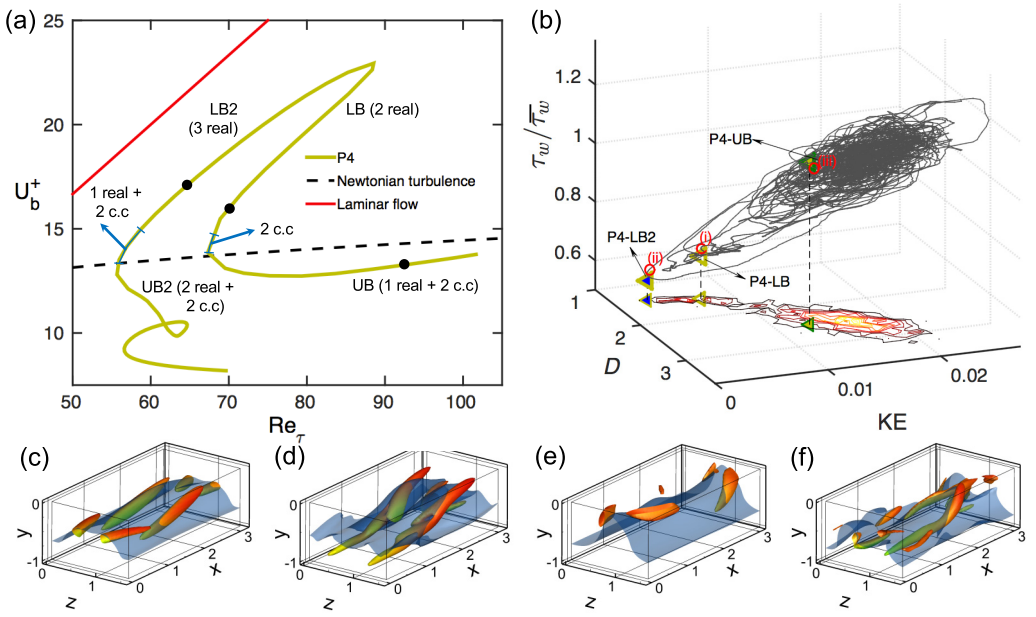

FIG. 1. (a) Bifurcation diagram for P4 traveling wave solutions along with curves for Newtonian turbulence and laminar flow [38], where the bulk velocities U_b^+ are plotted as a function of the friction Reynolds number. The number of unstable eigenvalues is indicated on each branch. Dots on each branch correspond to P4 TW solutions shown in panel (b). (b) State-space visualization at $\mathrm{Re}_c = 1800$, projected onto disturbance kinetic energy (KE), energy dissipation rate (D) and normalized instantaneous wall shear stress ($\tau_w/\bar{\tau}_w$) [38]. The gray line indicates a turbulent trajectory. A joint probability function of KE and D for the trajectory is shown at the bottom of the figure. The labeled symbols ($\lhd$) are P4 solutions at $\mathrm{Re}_c = 1800$. Based on the L_2 distance between the trajectories and P4 traveling waves [38], the closest visits to P4-LB, P4-LB2, and P4-UB are at points (i), (ii), and (iii), respectively. All quantities are calculated only for the bottom half of the channel. (c)–(f) Vortical structures illustrated by the swirling strength λ_{ci}. (c) P4-LB, (d) P4-UB, (e) instant (i), and (f) instant (iii). For panels (c) and (d), the tubes are isosurfaces at 2/3 of the maximum swirling strength. The maximum swirling strengths are (c) 0.30 and (d) 0.79. The isosurfaces are colored based on the local value of the streamwise velocity, ranging from low (blue) to high (red). The transparent blue isosurfaces indicate critical layer surfaces where the local streamwise velocity matches the wave speed of the solution. For the flow structures in panels (e) and (f), we use the same vortex strength and critical isosurfaces as in panels (c) and (d), respectively.

such as strong streamwise vortices and three-dimensionality and a mean velocity profile near the von Kármán profile, and "hibernating" intervals, with very low drag characteristics such as very small Reynolds shear stress and a mean velocity profile approaching the so-called "maximum drag reduction" asymptote first identified by Virk [41,42] for drag-reducing polymer solutions. Similar observations have been made by Hamilton *et al.* in plane Couette flow [3] and Weber *et al.* [43] in channel flow. The latter work performed Karhunen-Loéve decomposition of minimal channel results, identifying a small number of turbulent burstlike events called "entropy events" preceded by a time interval during which flow is dominated by streamwise-invariant "roll modes." Park and Graham [38] clearly showed that this stochastic cycle is a reflection of the organization of the turbulent dynamics around a family of nonlinear traveling wave solutions [the "P4" family described below and illustrated in Fig. 1(b)]. Indeed, the hibernating intervals are approaches to P4 lower branch solutions, while the active intervals are close to P4 upper branch solution. Recently, Kushwaha *et al.* [44] showed the relationship between temporal hibernating dynamics in minimal channels and spatiotemporal hibernating dynamics in extended domains. They partitioned the flow characteristics in extended domains into low, intermediate, and high drag classes. They performed both temporal and spatial

analyses on turbulent velocity fields of these three classes in an extended domain or real turbulence. The differences between these classes were presented by examining mean velocity, wall shear stress, and flow structures. Interestingly, the temporal and spatial analyses yielded very similar results for the low and high drag classes. The conditional mean profiles during low drag events occurring temporally and spatially in extended domains closely resemble those found in temporal hibernating intervals in the minimal channel as well as P4 lower branch solution. Thus, these results suggest that the temporal hibernating dynamics in a minimal domain is closely related to the spatiotemporal dynamics of low drag events in real turbulence or an extended domain.

One important issue regarding exact coherent states is their connection to critical layer dynamics. Recall from classical linear stability theory for shear flows that the Orr-Summerfeld equation in the inviscid limit has a singular point at a location called the *critical layer* where the streamwise velocity of the base flow is the same as the wave speed of a velocity perturbation of normal mode form $\hat{\boldsymbol{u}}(y)\exp[i(k_x x + k_z z) - ct]$ [45]. Wang *et al.* [46] showed for Couette flow that at least one lower branch ECS solution has a flow structure that consists of streaks, rolls, and a weak streamwise-varying wave that develops a critical layer; i.e., their flow structures are highly localized around the surface where the local streamwise velocity matches the wave speed of the ECS. Based on a scaling analysis, they suggested that the wavy fluctuations should be localized in a critical layer of depth $O(\mathrm{Re}^{-1/3})$, showing that this scaling was followed by their numerical solutions. As the critical layer is approached, the wavy fluctuation increases so the maximum fluctuation takes place in the critical layer. In fact, it is found that the flow structures at $\mathrm{Re} = 50\,000$ and $\mathrm{Re} = 3000$ were virtually identical modulo a $\mathrm{Re}^{1/3}$ rescaling of the direction normal to the critical layer surface. Hall and coworkers [21,47] used a mixture of asymptotics and numerics to show, again for Couette flow, that velocity fluctuations with wave vector in the flow direction are amplified in the critical layer and serve as forcing for the streamwise rolls to generate the nonlinear self-sustaining process that supports exact coherent states. In their formulation, this process is a self-sustaining version of wave-vortex interaction identified earlier by Hall in the context of three-dimensional instability of Görtler vortices [48]. Although the importance of the nonlinear critical layer mechanism becomes clearer at much higher Reynolds number [47,49,50], Hall and Sherwin [47] showed that "remarkable" agreement is obtained between the high Re asymptotics and the numerical results down to Reynolds numbers of $O(10^3)$. Other interesting work on nonlinear critical layers and ECSs has been performed by Viswanath in pipe flow [49] and Gibson and Brand in channel flow [51]. More recent work for channel flow [38] showed that at least two ECS solution families including the P4 family mentioned above display nonlinear critical layer dynamics—fluctuations are closely organized around the critical layer, from which observation these ECS families are called "critical layer modes." Other ECS solution families are found to display a different structure, in which fluctuations are largest near the channel center. As such, these are denoted as "core modes." More generally, Deguchi and Hall [52] observe that the alignment of the vortical structures around the critical layer are not necessarily found for upper branch ECSs, especially for large streamwise wavelengths. It is worth noting that lower branch TW solutions previously found in Couette flow [21,46,47], pipe flow [49], and channel flow [51] would be classified as critical layer modes rather than core modes.

Other work that is relevant to the present discussion is that of McKeon and Sharma [53], which builds on the idea that the full dynamics of a turbulent shear flow can be well approximated using a small number of modes that derive from the singular value decomposition of the resolvent operator corresponding to the Navier-Stokes operator linearized around a chosen mean velocity profile. As in classical linear stability theory, the modes have the form of traveling waves $\hat{\boldsymbol{u}}(y)\exp[i(k_x x + k_z z) - ct]$ and the critical layer for a given traveling wave is the wall-normal position where the mean velocity equals c. The convective nonlinear term enters the linear system as a forcing term. Resolvent modes have been used to represent several significant features of wall turbulence, including hairpin packet structure, skewness, and amplitude modulation behavior, and a formalization of the attached eddy hypothesis for which several highly amplified modes are linearly superimposed [54]. Recently, it has been shown that many ECS can be well represented by just a few resolvent modes [55].

In this paper, we present an analysis of turbulent dynamics in a minimal channel, with an emphasis on the connection to exact coherent states. We will also address one specific question about the existence of characteristic frequencies associated with critical layer dynamics in turbulent flows. The critical layer frequencies in turbulence will be identified, with use of nonlinear traveling wave solutions whose fluctuations display critical layer dynamics. The problem formulation is presented in Sec. II. Nonlinear traveling wave solutions that display critical layer dynamics are presented in Sec. III A, where their instability and bifurcation scenarios are discussed. Section III B illustrates temporal coherence of turbulent dynamics, composing of bursting and critical layer frequencies in a turbulent flow. Sections III C and III D describe the connections between hibernating turbulence, turbulent bursts, and the instability of traveling wave solutions. Section IV presents conclusions.

II. PROBLEM FORMULATION

We consider an incompressible Newtonian fluid in the plane Poiseuille (channel) geometry, driven with a constant volumetric flow rate. The x, y, and z coordinates are aligned with the streamwise, wall-normal, and spanwise directions, respectively. Periodic boundary conditions are imposed in the x and z directions with fundamental periods L_x and L_z, and no-slip conditions are imposed at the walls $y = \pm h$, where $h = L_y/2$ is the half-channel height. Using the half-height h of the channel and the laminar centerline velocity U_c as the characteristic length and velocity scales, respectively, the nondimensionalized Navier-Stokes equations are then given as

$$\boldsymbol{\nabla} \cdot \boldsymbol{u} = 0, \tag{1}$$

$$\frac{\partial \boldsymbol{u}}{\partial t} + \boldsymbol{u} \cdot \boldsymbol{\nabla} \boldsymbol{u} = -\boldsymbol{\nabla} p + \frac{1}{\mathrm{Re}_c} \nabla^2 \boldsymbol{u}. \tag{2}$$

Here, we define the laminar equivalent Reynolds number for the given flow rate as $\mathrm{Re}_c = U_c h/\nu$, where ν is the kinematic viscosity of the fluid. We fix the bulk velocity at the laminar value $U_b = 2U_c/3$ (or simply 2/3 in our nondimensionalization). Characteristic inner scales are the friction velocity $u_\tau = (\bar{\tau}_w/\rho)^{1/2}$ and the near-wall length scale or wall unit $\delta_\nu = \nu/u_\tau$, where ρ is the fluid density and $\bar{\tau}_w$ is the time- and area-averaged wall shear stress. As usual, quantities nondimensionalized by these inner scales are denoted with a superscript +. The friction Reynolds number is then defined as $\mathrm{Re}_\tau = u_\tau h/\nu = h/\delta_\nu$.

Simulations are performed using the open source code CHANNELFLOW, written and maintained by Gibson [56]. In this study, we focus on the domain $L_x \times L_y \times L_z = \pi \times 2 \times \pi/2$, the same box size as the P4 solution family [38]. A numerical grid system is generated on $N_x \times N_y \times N_z$ (in x, y, and z) meshes, where a Fourier-Chebyshev-Fourier spectral spatial discretization is applied to all variables. A typical resolution used is $(N_x, N_y, N_z) = (48, 81, 48)$.

The exact coherent states studied here have two important symmetries: They are reflection symmetric across the center plane of the channel $y = 0$ and across a plane of constant z. There are, of course, other ECS that do not obey these symmetries (e.g., Refs. [29,30,51,57,58]); we focus on these states because of their previously demonstrated connection to the turbulent dynamics [38], which we further discuss below. All simulations of turbulent trajectories reported here are performed without imposing any symmetries on the flow field.

III. RESULTS AND DISCUSSION

Prior to proceeding to the results, the definitions for the two temporally intermittent phenomena of interest here, hibernation and turbulent burst, are necessary. The criterion for a particular event is that the spatially averaged quantity must pass through a threshold value and stay on the same side of the threshold for a specified minimum time duration. We define a hibernation event [39,59,60] as occurring when the area-averaged wall shear stress drops below 90% of the mean wall shear stress and stays there for a certain duration $tU_c/h > 65$. At $\mathrm{Re}_c = 1800 (\mathrm{Re}_\tau = 85)$, the duration

threshold $tU_c/h > 65$ corresponds to $t^+ = 260.9$, where $t^+ = tu_\tau^2/\nu$ is time scaled in inner units. Note that this duration threshold also corresponds to $t^* > 3$, where $t^* = tu_\tau/h$ is time scaled with eddy turnover time. This threshold value of $t^* > 3$ was previously used to detect hibernation events in experimental and computational studies [44,61]. We define a bursting event as occurring when the volume-averaged energy dissipation rate (D) increases by 1.5 times its standard deviation (σ_D) for a duration $tU_c/h > 15$. Note that the typical time duration of a bursting process is $O(10h/U_c)$ [35]. The choice of the cutoff duration for hibernating and bursting events were tested. Selecting $tU_c/h > 55(t^+ > 220.8)$ or $tU_c/h > 75(t^+ > 301)$ for a hibernation event [44,61] and $tU_c/h > 12.5$ or 17.5 for a bursting event gives almost identical results.

A. Traveling wave solutions: Instability and turbulent attactors

Park and Graham [38] found that the dynamics of minimal channel turbulence are organized at least in part around the P4 solution family, so these ECS solutions are the focus of the present study. It is, however, worth mentioning that there may exist other ECSs with different flow symmetries in the same computational domain at the same Reynolds numbers, which may also play a role in organizing the turbulent attractor. Figure 1(a) presents a bifurcation diagram for P4 solutions on a Prandtl–von Kármán plot. This form is often used to represent drag reduction characteristics in wall-bounded turbulent flows. The bulk velocities U_b^+ are plotted as a function of the friction Reynolds number along with curves for Newtonian turbulence and laminar flow. In this representation, a lower branch (LB) solution is above a upper branch (UB) solution, because the former has higher bulk velocity for the same wall shear stress than the latter. All P4 solutions exhibit reflection symmetry with respect to the midplane in the spanwise direction, $z = L_z/2$, and wall normal direction, $y = 0$. A brief summary of the bifurcation behavior of the P4 solution family is as follows. Starting from the P4-UB solution at the upper range of convergence $\mathrm{Re}_\tau \approx 100$ whose branch has a mean velocity close to that of Newtonian turbulence and a varicose streak structure, the solution remains close to the Newtonian turbulence curve until it reaches a turning point at $\mathrm{Re}_\tau = 67.32$ with decreasing Re. Beyond this turning point, the solution branch, which we now denote LB, becomes nearly parallel to the laminar solution as Reynolds number increases, but turns around again at $\mathrm{Re}_\tau = 88.7$, forming another lower-branch solution called LB2. As Reynolds number decreases, the streak structure changes from varicose to sinucose and the branch reaches another saddle-node bifurcation point at $\mathrm{Re}_\tau = 55.63$, beyond which we call the solution UB2. This solution branch ends at $\mathrm{Re}_c = 855$, where it collides in a pitchfork bifurcation with a higher symmetry solution branch [62], which satisfies an xz-shift symmetry condition

$$[u \quad v \quad w](x,y,z) = [u \quad v \quad w](x + L_x/2, y, z + L_z/2).$$

The bifurcation scenario for the P4 solution family is investigated with use of the linear stability analysis. The leading eigenvalues of the solutions are computed in their symmetric subspace with Arnoldi iteration [37]. It is found that far away from the UB-LB bifurcation points, the P4-LB and P4-LB2 solutions have two and three real unstable eigenvalues, respectively. Note that in the full state space, the P4-LB and P4-LB2 additionally possess one real and four complex conjugate unstable eigenvalues. The turning point scenario from the P4-LB to the P4-UB is as follows. Near the bifurcation point on the P4-LB branch, two real unstable eigenvalues collide at a location away from the imaginary axis and become complex conjugates. At the saddle-node bifurcation, a real eigenvalue becomes positive. Thus, the P4-UB solution has one real and two complex conjugate unstable eigenvalues. In the case of the turning point from P4-LB2 to P4-UB2, the scenario is slightly different. As the P4-LB2 closely approaches the bifurcation point $\mathrm{Re}_\tau = 55.63$, the two unstable eigenvalues approach each other, while the most unstable eigenvalue is still away from the two unstable ones. Near the bifurcation point, the two real unstable eigenvalues collide and become complex. At the bifurcation point, a real eigenvalue (i.e., the bifurcating eigenvalue) crosses the imaginary axis, adding a unstable eigenvalue to the P4-UB2. The P4-UB2 solution then has two real and one complex conjugate pair of unstable eigenvalues. This is not a Takens-Bogdanov bifurcating

scenario [63], which is associated with two eigenvalues that may change from real to complex near a saddle-node bifurcation involving one of them. It is worth mentioning, however, that some TW solutions in pipe flow [64], channel flow [38], and plane Couette flow [65] exhibit this type of bifurcation.

To address connections between the P4 solution family and turbulent trajectories in a minimal domain, Park and Graham [38] presented the state-space dynamics, projecting turbulent trajectories along with the P4 solutions onto a three-dimensional subspace, as illustrated in Fig. 1(b). The DNS and P4 solutions are shown at $\mathrm{Re}_c = 1800$. The three-dimensional space is constructed by disturbance kinetic energy (KE), energy dissipation rate (D), and area-averaged instantaneous wall shear stress normalized by its mean value ($\tau_w/\bar{\tau}_w$). In addition, the joint probability density function (PDF) of KE and D is shown at the bottom of the figure. All quantities are only calculated for the bottom half of the domain. It is worth mentioning that, as opposed to the computation of TW solutions, the turbulence simulations are performed without imposing any symmetries on the flow. The dynamical trajectory spends most of its time orbiting in the vicinity of the P4-UB solution. The trajectory occasionally escapes from the neighborhood of the P4-UB, approaching the P4-LB solutions. To quantify the closest visit to the P4 solutions, the L_2 norm of the difference between a DNS velocity field and a P4 is calculated [38]. Points (i)–(iii) indicate the closest visits to P4-LB, P4-LB2, and P4-UB, respectively. The returning trajectories after close visits to P4-LB solutions are closely related to the bursting process [34,35], which will be further discussed in Sec. III D.

Flow structures of P4-LB and P4-UB are shown in Figs. 1(c)–1(d). Only the bottom half-channel is shown due to the mirror symmetry with respect to the channel center. The structures are illustrated by isosurfaces of swirling strength λ_{ci}, the imaginary part of the complex conjugate eigenvalues of the velocity gradient tensor [66]. Values are given in the caption. We also depict the critical layer surface, where the local streamwise velocity matches the wave speed. The P4-LB and P4-UB solutions exhibit vortex cores closely located around the critical layer. To facilitate comparison, the same vortex strength and critical layer isosurfaces as in Figs. 1(c) (P4-LB) and 1(d) (P4-UB) are used for flow structures for instants (i) and (iii), as visualized in Figs. 1(e) and 1(f), respectively. Strong similarity is observed in the vortical and critical layer structures between the P4 solutions and DNS snapshots. Interestingly, in the turbulent flow the vortical motions are also observed to be localized around the critical layer displayed by the P4 solutions.

Before continuing, it should again be mentioned that other ECS families besides P4, perhaps with different symmetries, may play a role in the turbulent dynamics in the computational domain we consider. The P4 family studied has mirror symmetries about the midplanes in the x and z directions, while turbulence simulations are not subject to any symmetries on the flow.

B. Temporal coherence of turbulent dynamics: Bursting and critical layer frequencies

We now turn our attention to the temporal coherence of turbulent dynamics. The aim is to identify characteristic frequencies related to bursting and critical layer dynamics in a minimal channel flow. To this end, Fourier analysis is applied to time series of turbulence quantities. Figure 2(a) shows a time series of the energy dissipation rate (D) at $\mathrm{Re}_c = 1800$ ($\mathrm{Re}_\tau = 85$) in a minimal channel along with the mean (black dashed line) and the mean + 1.5 times its standard deviation (red dotted line). Temporally intermittent behavior of the energy dissipation rate is clearly discernible. This intermittent dynamics is closely related to temporal coherence of the turbulent flow—a bursting event. The characteristic intermittent cycle or burst period can be identified more readily by the power spectral density of the time series. Figure 2(b) shows the power spectrum of the energy dissipation rate of a sufficiently long simulation run (more than 2×10^4 h/U_c), where it is normalized to have the maximum of 1. The dominant frequency ω_d in the spectrum corresponds to the characteristic burst period, i.e., $T_d = 2\pi/\omega_d$. Figure 2(c) shows the length of the burst period T_d (blue circles) calculated by the dominant frequencies in the power spectra at different Reynolds numbers. The burst interval T_b, which is the mean time between individual bursts, can be also calculated by the aforementioned definition for a bursting event and is presented in red squares in Fig. 2(c). Both bursting time scales

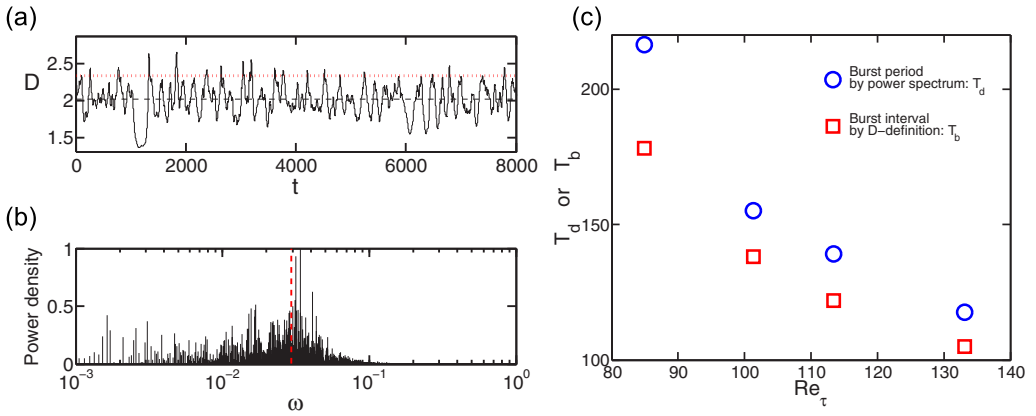

FIG. 2. (a) Time series of the energy dissipation rate (D) at $\mathrm{Re}_c = 1800$ ($\mathrm{Re}_\tau = 85$) in a minimal channel flow. The black dashed and red dotted lines are the mean and the mean + 1.5 times its standard deviation, respectively. (b) Power spectral density of a long data set of D (more than $2 \times 10^4 h/U_c$). (c) Reynolds number dependence of characteristic burst periods computed from the power spectrum (blue circles) and by the definition of a turbulent burst (red squares). The red line in panel (b) is $\omega_b = 2\pi/T_b$, where T_b is the mean burst interval (red square) in panel (c).

(blue and red symbols) are close each other and show the same trend with respect to Reynolds number. In particular, with viscous inner scales, the bursting intervals in Figure 2(c) are $O(10^3)$, which is consistent with those of Jiménez *et al.* [5] for minimal Poiseuille flows. In Fig. 2(b), the bursting frequency calculated by our selected criteria for a turbulent burst (red squares), i.e., $\omega_b = 2\pi/T_b$, is shown—it is very close to the dominant frequency of the time series. Note that the bursting in the minimal channel has also been shown to represent the bursting in real turbulence by examining the temporal statistics compiled in minimal sub-boxes in an extended domain [5]. However, the relationship between the temporal dynamics of the bursting in a minimal channel and the spatiotemporal dynamics of the bursting in real turbulence will be included in future work.

The bursting frequencies in Fig. 2 have been calculated using a spatially averaged quantity in the minimal channel. As shown in Fig. 2(b), the power spectrum of spatially averaged quantity nicely captures characteristic frequencies in a low-frequency regime of $\omega < 10^{-1}$. However, area averaging serves as a low-pass filter and for the nonlinear traveling wave solutions, all area-averaged quantities are constant. Therefore, we now consider time series of instantaneous velocities sampled at a point in a channel. As a prelude to this discussion, we recall that the ECS family under consideration here has dynamics and structure that are closely associated with a critical layer where the wave speed equals the local streamwise velocity [38]. To infer the frequency associated with any wave, the wave speed c and the wavelength λ are related to the frequency ω by $\omega = 2\pi c/\lambda$. For the ECS considered here in the minimal channel, the wavelength $\lambda = L_x$ and the wave speed is c_x, so the frequency of a specific ECS is given by $\omega_c = 2\pi c_x/L_x$. We will variously denote this as the "ECS frequency" or "critical layer frequency," using the latter when the connection to critical layer structure and dynamics is to be emphasized. Finally, because the three-dimensional instability of the streaks induced by the streamwise vortices is a key aspect of the self-sustaining process underlying ECS and near-wall turbulence, the ECS frequency might also be described as a "streak instability frequency." It is worth noting that the dominant streamwise wavelength of the streak instability and the streamwise vortices is $\lambda_x^+ \simeq 200$–300 in large domain simulations [67,68], which is close to the streamwise wavelength of the P4 family. Figures 3(a) and 3(b) show the wave speed of the P4 solution family as a function of the Reynolds number in outer and inner units. The laminar bulk velocity, U_b, is also plotted with a dashed line. The wave speeds of the P4 solutions vary and the solutions have a larger wave speed than the laminar bulk velocity in outer units, and vice versa in inner units. In Fig. 3(b), P4-UB solutions

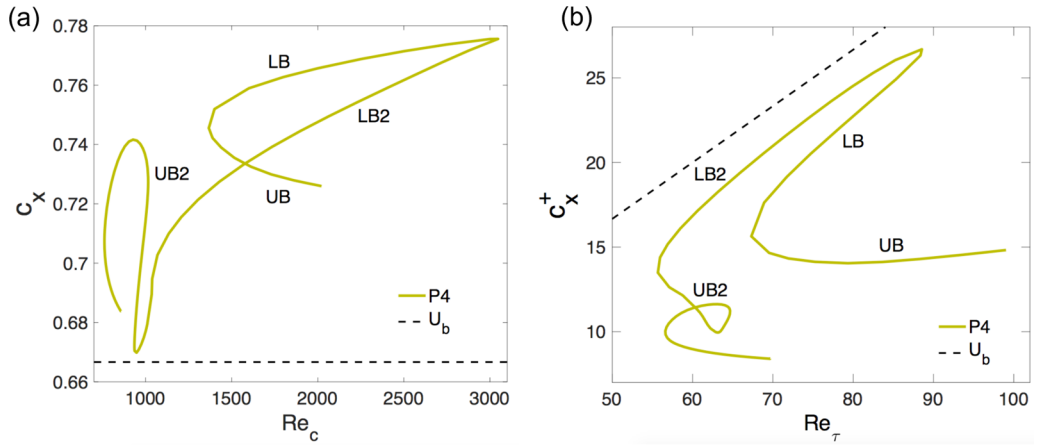

FIG. 3. Wave speed for the P4 traveling wave solutions as a function of the Reynolds number in (a) outer units (i.e., scaled with U_c and plotted against Re_c) and (b) inner units (i.e., scaled with u_τ and plotted against Re_τ). The laminar bulk velocity, U_b, is plotted with a dashed line.

display $c_x^+ \sim 14$–15 in the range considered here, which is slightly larger than the result $c_x^+ \sim 10$–12 reported for the propagation speed of near wall structures [69].

Figure 4 shows the power spectral densities of pointwise-sampled velocities in DNS along with the frequencies displayed by the P4 solutions and the bursting frequency calculated from burst intervals

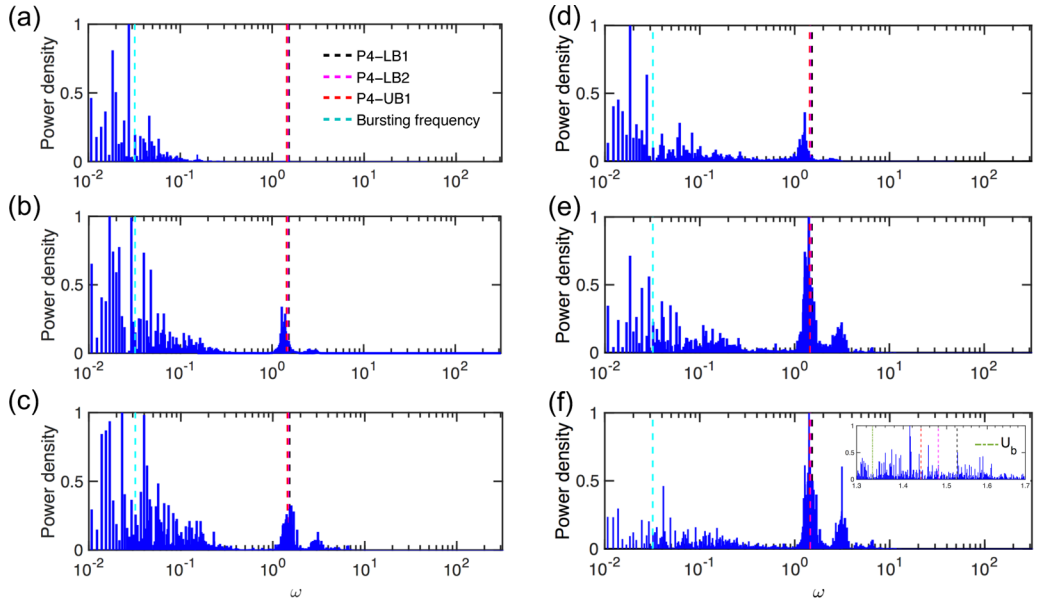

FIG. 4. Power spectral density of a pointwise-sampled velocity at $\mathrm{Re}_c = 1800$ ($\mathrm{Re}_\tau = 85$) in the channel domain. [(a)–(c)] Power spectra of the streamwise velocity at $y^+ = 5,49,65$ and [(d)–(f)] power spectra of the wall-normal velocity at $y^+ = 5,49,65$, along with the critical layer frequencies and bursting frequency. The relevant critical layer frequency ($\omega_c = 2\pi c_x / L_x$) is calculated using the wave speed (c_x) of P4 traveling wave solutions, and the bursting frequency ($\omega_b = 2\pi / T_b$) is calculated using the burst interval T_b (red square) in Fig. 2(c).

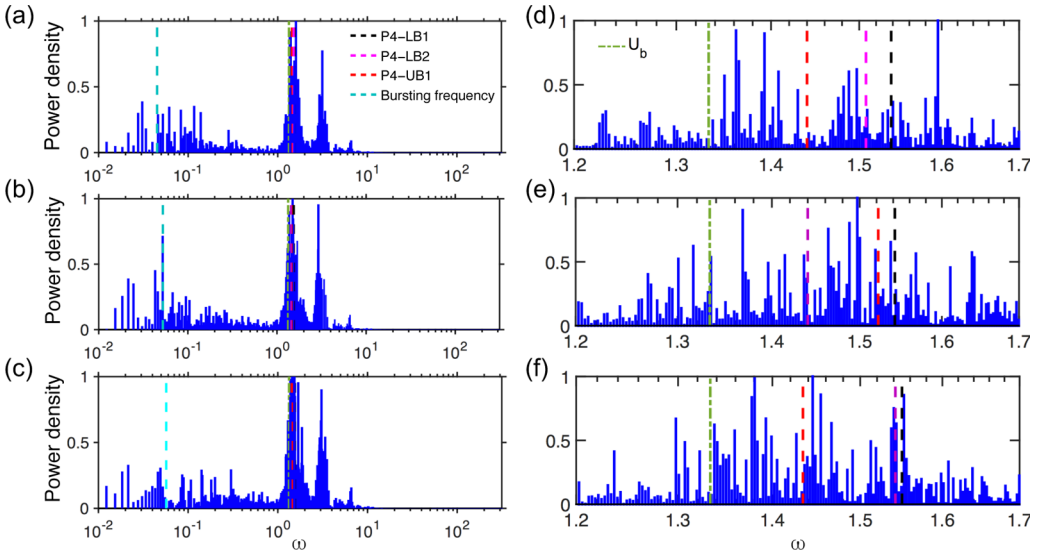

FIG. 5. Reynolds number dependence of the power spectra of wall-normal velocities at $y = 0.23$ (note that $y = 0$ corresponds to the channel center). [(a)–(c)] Power spectra at $\mathrm{Re}_\tau = 101$ ($y^+ = 77$), at $\mathrm{Re}_\tau = 113$ ($y^+ = 87$), and at $\mathrm{Re}_\tau = 133$ ($y^+ = 102$), respectively. [(d)–(f)] Enlargement of power spectra for the frequency regime of $1.2 < \omega < 1.7$ at $\mathrm{Re}_\tau = 101$ ($y^+ = 77$), at $\mathrm{Re}_\tau = 113$ ($y^+ = 87$), and at $\mathrm{Re}_\tau = 133$ ($y^+ = 102$), respectively. An additional line for the frequency ω_m corresponding to the laminar bulk velocity U_b is shown.

in Fig. 2(c). The DNS and P4 solutions are at $\mathrm{Re}_c = 1800$ ($\mathrm{Re}_\tau = 85$). The frequencies of P4-LB, LB2, and UB are all plotted, but they are very close each other. The bursting frequency is from the mean burst interval [red squares in Fig. 2(c)], i.e., $\omega_b = 2\pi/T_b$. Figures 4(a)–4(c) show the power spectra of the streamwise velocities at $y^+ = 5,49,65$, respectively. At all these positions, there are dominant frequencies in the range of $0.01 < \omega < 0.05$ in which the bursting frequency is located. Near the wall, as shown in Fig. 4(a), the turbulence barely displays signals near the ECS frequencies. As we move away from the wall, small peaks start to appear near the ECS frequencies. The dominant frequencies depicted in the power spectra are closely related to the bursting frequencies reported in experimental and numerical turbulence studies [70,71]. Frequencies close to the ECS frequencties are, however, more evident for the wall-normal velocities. Figures 4(d)–4(f) show the power spectra of the wall-normal velocities at $y^+ = 5,49,65$, respectively. In Fig. 4(d), near the wall there is still a dominant frequency in the range of $0.01 < \omega < 0.03$ in which the bursting frequency is located. But the turbulence also displays a small peak near the ECS frequencies. Furthermore, peaks close to the ECS frequencies become more significant in the spectrum as we move away from the wall—the dominant peak location is switched from the low frequency regime ($\omega < 10^{-1}$) to a higher frequency regime ($\omega > 10^{-1}$). In other words, the critical layer frequency becomes predominant over the bursting frequency. In both the $y^+ = 49$ and 65 cases, the peak frequency in the regime $\omega > 10^{-1}$ is very close to the ECS frequencies. Indeed, it becomes more prominent as further moved away from the wall. It should be noted that a pointwise sampled streamwise and wall-normal velocities well capture the bursting frequency calculated from the volume-averaged energy dissipation rate, without reference to traveling wave solutions. The central point is that the turbulence exhibits frequencies very close to the critical layer frequencies found in the P4 solution family and they are the most prominent near the channel center.

Now the dependence of the Reynolds number on the power spectrum is investigated. Figures 5(a)–5(c) show the power spectra of the wall-normal velocities sampled at a point near the channel center ($y = 0.23$) at $\mathrm{Re}_\tau = 101,113$ and 133, respectively. As Reynolds number increases, frequencies near the ECS frequencies become more prominent and are still well captured by P4

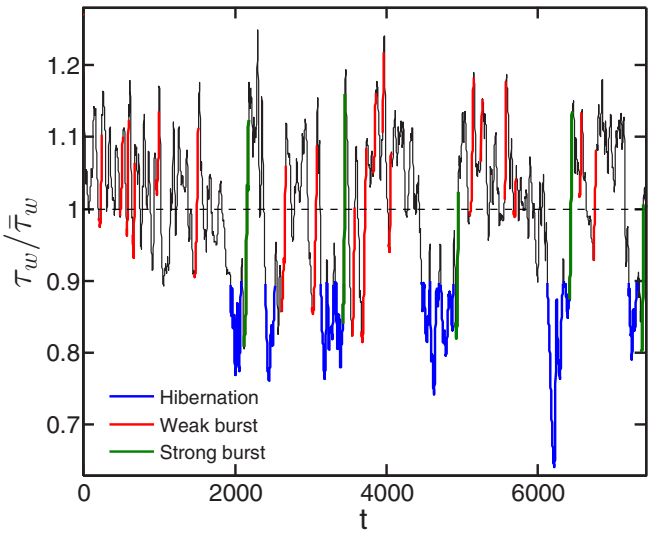

FIG. 6. Time series of the area-averaged wall shear stress normalized by its time average value (black dashed line) as a function of time t. Shown are hibernating turbulence (blue intervals), bursting events after hibernation (green intervals), and other bursting events not associated with hibernation (red intervals).

solutions. Furthermore, the second harmonics of these frequencies (i.e., frequencies near $2\omega_c$) appear to become more noticeable with increasing Reynolds number.

Finally, of course there is a frequency $\omega_m = 2\pi U_b/L_x$, where U_b is the laminar bulk velocity. This will be close to the ECS and critical layer frequencies for the simple reasons that the wave speeds for the ECS are close to (but slightly higher than) U_b and the wavelengths of the ECS are all L_x. Figures 5(d)–5(f) show enlargements of plots from Figs. 5(a)–5(c) for the range of $1.2 < \omega < 1.7$ with an additional line indicating ω_m. There appear to be signals around the frequency for the bulk mean velocity, but the dominant frequencies are still closer to the critical layer frequencies of the P4 solutions. Moreover, the prominence of the critical layer frequency over the frequency for the bulk mean velocity becomes more noticeable as the Reynolds number increases, where dominant peak frequencies are located very close to the critical layer frequencies of P4-LB, LB2, and UB solutions.

C. Hibernation and bursting process

In this section, we investigate the relationship between a hibernation-induced intermittency and turbulent bursts. Figure 6 shows a time series of the area-averaged shear rate measured at the top wall. During intervals denoted by blue lines, the wall shear rate satisfies our criteria for a hibernation event. Having defined a burst event as a large enhancement of the energy dissipation rate, the wall shear stress substantially increases during bursting intervals (red and green intervals). Especially for bursting events occurring after hibernating intervals (green intervals), the wall shear stress appears to rise more substantially, compared with the other bursting events not associated with hibernation (red intervals), suggesting that there are very strong flow motions near the end of hibernating intervals. We quantify this observation below.

To closely examine what happens around the end of hibernation events, we perform conditional sampling of the wall shear stress for hibernation events. In Fig. 7, conditionally sampled instantaneous wall shear stress events during intervals of hibernating turbulence (gray lines) are shown at $\mathrm{Re}_c = 1800$ ($\mathrm{Re}_\tau = 85$). These are shifted so that the ending time of the hibernation is placed at $t = 0$ at which the wall shear stress is 10% below the mean (black dashed line). Also shown is the ensemble average wall shear stress of the hibernation events (thick red line). The vertical dotted line corresponds

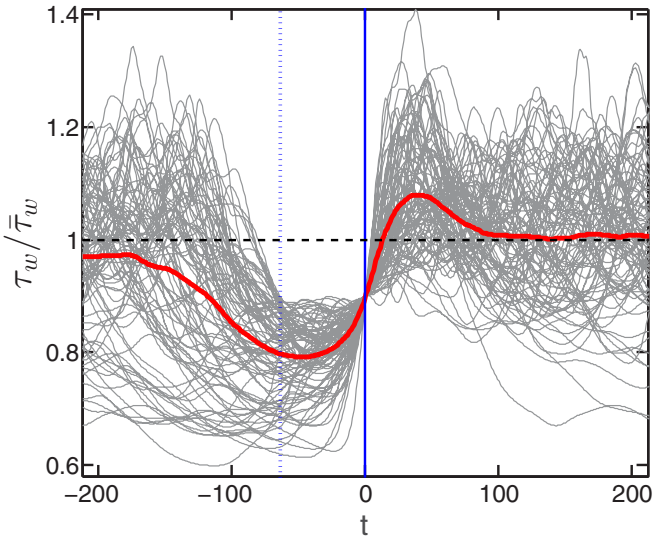

FIG. 7. Conditionally sampled instantaneous wall shear stress events (gray lines) during intervals of hibernating turbulence at $\mathrm{Re}_c = 1800$ ($\mathrm{Re}_\tau = 85$). The ensemble-averaged profile and the unconditional mean wall shear stress are shown by the red line and black dashed line, respectively. The time origin of each event is shifted so that its end corresponds to $t = 0$ (vertical blue line). The vertical blue dotted line denotes $t = -65$, which is the minimum time duration of a hibernation event based on our criteria.

to $t = -65$, which is the time duration for hibernation. On average, there is a considerable increase of the wall shear stress about 30% after the end of hibernation—there is a very strong turbulent activity, which is eventually related to the bursting process. For comparison, a typical increase of the wall shear stress during bursting intervals is around 15% in our simulation. This observation leads us to classify bursting events with respect to hibernation events. In the nomenclature of the present work, if there is a turbulent burst after a hibernation event, it will be called a "strong" burst, while the remainder will be denoted relatively "weak." From this classification of bursts, it is reasonable to expect that the strongest bursts follow hibernation (which as we will see below, is the conclusion that we ultimately draw).

Figure 8(a) shows the probability density function of the increase of the energy dissipation rate (ΔD) during burst intervals in a minimal channel simulation at $\mathrm{Re}_\tau = 85$, where the PDF is normalized so that its area integral is 1. The increase of the energy dissipation rate can be considered as the magnitude of bursting events. As hibernation and bursting events are identified by our selected criteria, strong and weak bursts can be easily classified. In Fig. 8(a), the PDF of the increase of the energy dissipation rate (ΔD) during strong and weak bursting intervals is shown. The ensemble-averaged magnitudes of strong and weak bursts are $\overline{\Delta D} = 0.82$ and $\overline{\Delta D} = 0.43$, respectively. Figure 8(b) shows the average magnitude of turbulent bursts normalized by a standard deviation of the energy dissipation rate in the range of $75 < \mathrm{Re}_\tau < 115$. As Reynolds number increases, the average magnitude of all bursts (both strong and weak bursts) appears to remain constant, while the average magnitudes of strong and weak bursts increase. However, the ratio between the average magnitudes of strong and weak bursts increases with increasing Reynolds number, suggesting that there are stronger bursts after hibernation at higher Reynold number.

It should be emphasized that although a hibernating interval does not necessarily lead to a turbulent burst, every "strong" bursting process is always preceded by hibernating turbulence in the limited range of Reynolds number studied here. Thus, hibernation can be a precursor to a very strong turbulent activity (i.e., strong burst), providing potentially significant information for flow control strategies.

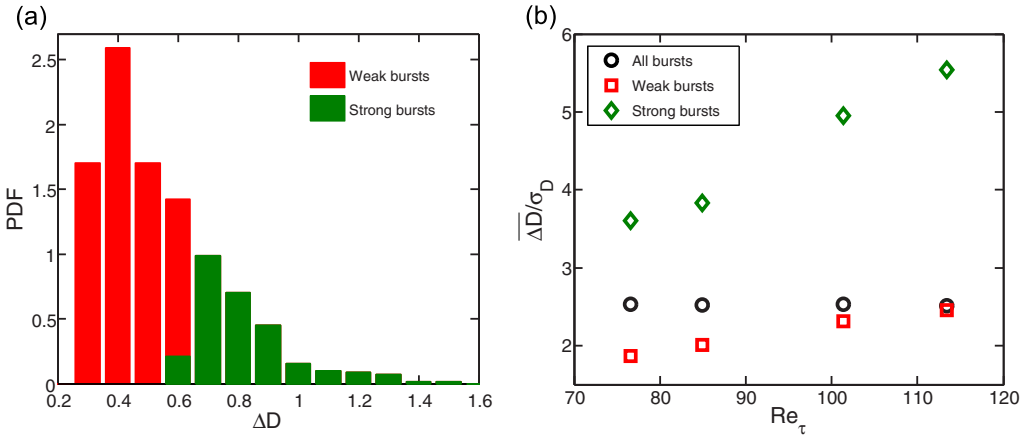

FIG. 8. Classification of turbulent bursts with respect to hibernation: strong and weak bursts. (a) Probability density function for the bursting magnitudes ΔD (defined as the increase of the energy dissipation rate) of two burst classes and (b) Reynolds number dependence of the ensemble-averaged bursting magnitudes normalized by the standard deviation of the energy dissipation rate.

D. Bursts and unstable manifolds of traveling waves

We turn now to the nonlinear dynamics of the bursting phenomenon. As illustrated by Park and Graham [38], the hibernating intervals are approaches to P4-LB traveling wave solutions. Thus, it is reasonable that the trajectories of strong bursts may be very similar to those of points on the unstable manifolds of P4-LB solutions. Shown in Fig. 9(a) is the same plot as Fig. 1(b) along with trajectories of strong and weak burst classes. The length of trajectories of strong bursts is typically longer than that of weak bursts. The strong bursting trajectories (green lines) start their paths very close to P4 lower branch solutions and strongly overshoot the core region of the attractor—the P4-UB solution is near this core region. This overshooting behavior of the strong burst leads to a large drag increase.

Trajectories on the unstable manifolds of P4 lower branch solutions are illustrated in Fig. 9(b). As presented in Sec. III A, P4-LB, and P4-LB2 have two and three real unstable eigenvalues, respectively. A trajectory on the unstable manifold can be computed by integration of an initial condition perturbed along an unstable direction of a P4-LB solution. Figure 9(c) shows two and three trajectories on the unstable manifolds of P4-LB and P4-LB2, respectively. The strong bursting trajectories (green lines) in Fig. 9(a) look remarkably similar to those on the unstable manifolds of P4-LB solutions in Fig. 9(b).

These are not the first observations that a turbulent burst can be thought of as the escape process from an exact coherent state along its unstable manifolds [33–35]. Nevertheless, our observations provide specific details regarding the relationship between bursts and the unstable manifolds of several known ECS. Furthermore, along the unstable manifold of the most unstable eigenvalue of the P4-LB (blue line) is clearly seen a nearly heteroclinic connection between P4-LB and P4-UB solutions (at least as seen in this state space projection).

The time evolution of the flow structure along the most unstable direction of P4-LB shown in Fig. 9(c). The snapshots correspond to the dots in Fig. 9(b); the top snapshot is one close to P4-LB. Except for the last snapshot, which is very close to P4-UB, we use the same vortex strength and critical layer isosurfaces as for P4-LB in Fig. 1(c). Near the P4-LB solution, the flow structure still looks similar to that of P4-LB solution, where vortical motions are clearly organized around the critical layer. As the trajectory proceeds, the vortices appears to grow and thicken, while they seem to maintain the shape around the critical layer. As further moved away from the P4-LB, new vortices are generated, covering the whole channel domain. Nevertheless, vortices appear to be located around the critical layer. At the peak of the trajectory, i.e., the highest wall shear stress, some vortices

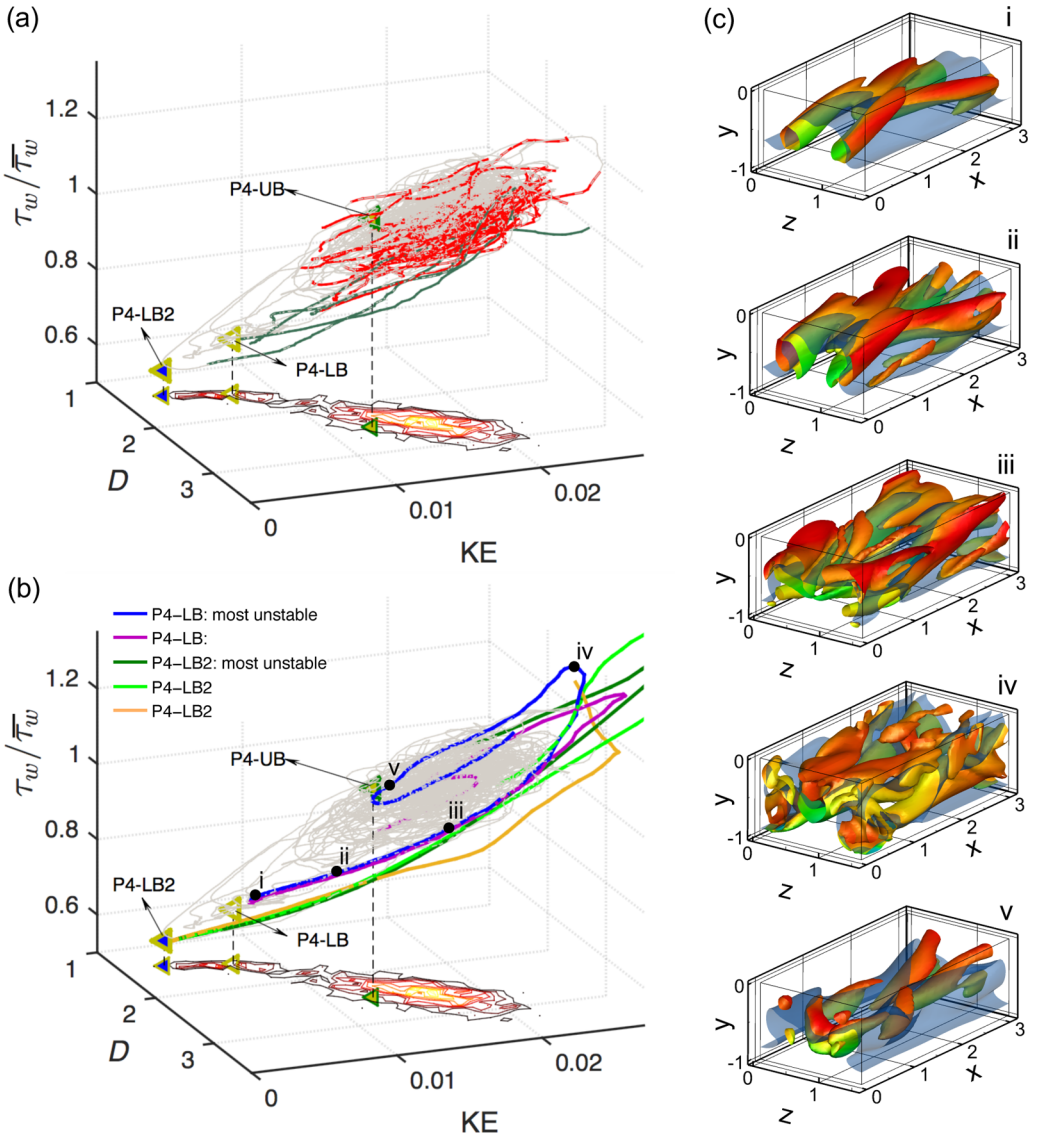

FIG. 9. [(a), (b)] State-space visualization of DNS trajectories and P4 solutions at $\mathrm{Re}_c = 1800$ ($\mathrm{Re}_\tau = 85$) projected onto three dimensions. The gray line indicates the turbulent trajectory. (a) The green and red lines represent trajectories of strong and weak bursts, respectively. (b) Trajectories of the unstable manifolds of the P4-LB solution are shown with blue and magenta lines, while those of the P4-LB2 solution are shown with light green, dark green, and pink lines. The solid circles correspond to the snapshots on the right. (c) Time evolution of flow structures along the most unstable manifold of the P4-LB indicated by dots in (b). Time marches downward. The tubes are isosurfaces at the swirling strength of 0.2, colored by the streamwise velocity u, 0 (blue) $\leqslant u \leqslant$ 1 (red). The transparent blue isosurfaces indicate critical layer surfaces where the local streamwise velocity matches the wave speed of the P4-LB solution.

break down into smaller ones. It should be noted that the structural evolution for the strong bursting trajectories is very similar to that in Fig. 9(c).

Using the temporal evolution of flow structure in Fig. 9(c), we attempt to describe the structural evolution in the context of the original description for a bursting process by Kline *et al.* [8]: streak

breakdown. In the top snapshot, Fig. 9(c), which is close to P4-LB, the isosurface is nearly streamwise invariant, showing a low-speed streak (the upward fold of the critical layer surface). As time marches, the isosurface, i.e., streak, becomes wavy and highly three-dimensional, developing inflectional instabilities. At approximately the same time, vortices begin to grow, and then the flow rapidly ends up being a chaotic motion, increasing drag sharply. In a nutshell, the temporal evolution along the unstable manifold of the P4 LB solution provides a very clear manifestation of streak breakdown during a bursting process.

Finally, revisiting the issue of a heteroclinic connection between P4-LB and P4-UB solutions, the last snapshot in Fig. 9(c) is illustrated by the same vortex strength and critical layer isosurfaces as the P4-UB solution in Fig. 1(c). The flow structure looks very similar to that of the P4-UB solution, where vortices are localized around the critical layer. The vortex legs are inclined by approximatively 38 deg with respect to the wall—the P4-UB shows about 40-deg inclined vortex legs. The maximum swirling strength of 0.72 is comparable to that of the P4-UB (0.79). The critical layer shape is also very similar to that of the P4-UB, showing similar streamwise variation as well as wall-normal position.

IV. CONCLUSION

We have investigated temporal coherence related to burst and critical layer dynamics in minimal turbulent channel flow and its connection to nontrivial invariant solutions to the Navier-Stokes equations called exact coherent states (ECS). We focus a family of ECS in a form of nonlinear traveling waves (TW) identified by Park and Graham [38], called P4 TW solutions, focusing on the linear instability and bifurcating scenarios near turning points. This solution family displays nonlinear critical layer dynamics; fluctuations are highly localized around the critical layer (the surface on which the local streamwise velocity coincides with the wave speed of the TW solution). A central observation of the present paper is that minimal channel turbulence displays distinct frequencies very close to the frequencies displayed by the P4-TW solution family, which in turn originate in the critical layer dynamics sustaining these solutions. The bursting frequency is predominant near the wall, while the critical layer (ECS) frequencies becomes predominant over the bursting frequency further from the wall. The latter are also more prominent at higher Reynolds number.

Another temporally intermittent phenomenon related to a low-drag events in minimal channel flow, denoted hibernating turbulence, and its relationship with a turbulent bursts are presented. Many of these low-drag events are followed by very strong turbulent activity: they are precursors to strong bursting events. In this regard, turbulent bursts are classified into strong and relatively weak classes with respect to hibernation. Defining the bursting magnitude as the increase of the energy dissipation rate during a bursting interval, the strong burst appears more than twice as strong as the weak burst in the range of $75 < \mathrm{Re}_\tau < 115$.

Finally we address the similarity between bursting trajectories and trajectories on the unstable manifolds of P4-LB solutions in state space. The latter comprises the instability of the P4-LB solutions and its nonlinear evolution. It is shown that the strong bursts display very similar trajectories to those of the P4-LB solutions, providing more direct evidence as to a connection of the bursting phenomenon to the instability of ECS [34,35]. Additionally, we identify a nearly heteroclinic connection between P4-LB and P4-UB solutions in state space.

ACKNOWLEDGMENTS

The authors gratefully acknowledge the financial support from the Air Force Office of Scientific Research through Grants No. FA9550-11-1-0094 and No. FA9550-15-1-0062 (Flow Interactions and Control Program) and from the National Science Foundation through Grants No. CBET-1066223 and No. CBET-1510291 (Fluid Dynamics Program). The direct numerical simulation code used here was developed and distributed by John Gibson at the University of New Hampshire.

[1] S. K. Robinson, Coherent motions in the turbulent boundary layer, Annu. Rev. Fluid Mech. **23**, 601 (1991).
[2] J. Jiménez and A. Pinelli, The autonomous cycle of near-wall turbulence, J. Fluid Mech. **389**, 335 (1999).
[3] J. Hamilton, J. Kim, and F. Waleffe, Regeneration mechanisms of near-wall turbulence structures, J. Fluid Mech. **287**, 317 (1995).
[4] J. Jiménez, How linear is wall-bounded turbulence? Phys. Fluids **25**, 110814 (2013).
[5] J. Jiménez, G. Kawahara, M. P. Simens, M. Nagata, and M. Shiba, Characterization of near-wall turbulence in terms of equilibrium and bursting solutions, Phys. Fluids **17**, 015105 (2005).
[6] J. Jiménez and P. Moin, The minimal flow unit in near-wall turbulence, J. Fluid Mech. **225**, 213 (1991).
[7] J. Jiménez, Near-wall turbulence, Phys. Fluids **25**, 101302 (2013).
[8] S. J. Kline, W. C. Reynolds, F. A. Schraub, and P. W. Runstadler, The structure of turbulent boundary layers, J. Fluid Mech. **30**, 741 (1967).
[9] S. C. C. Bailey, M. Vallikivi, M. Hultmark, and A. J. Smits, Estimating the value of von Kármán's constant in turbulent pipe flow, J. Fluid Mech. **749**, 79 (2014).
[10] G. J. Kunkel and I. Marusic, Study of the near-wall-turbulent region of the high-Reynolds-number boundary layer using an atmospheric flow, J. Fluid Mech. **548**, 375 (2006).
[11] J. Westerweel, G. E. Elsinga, and R. J. Adrian, Particle image velocimetry for complex and turbulent flows, Annu. Rev. Fluid Mech. **45**, 409 (2013).
[12] G. Borrell, J. A. Sillero, and J. Jiménez, A code for direct numerical simulation of turbulent boundary layers at high Reynolds numbers in BG/P supercomputers, Comput. Fluids **80**, 37 (2013).
[13] M. Lee and R. D. Moser, Direct numerical simulation of turbulent channel flow up to $\mathrm{Re}_\tau \approx 5200$, J. Fluid Mech. **774**, 395 (2015).
[14] P. Holmes, J. L. Lumley, G. Berkooz, and C. W. Rowley, *Turbulence, Coherent Structures, Dynamical, Systems and Symmetry*, 2nd ed. (Cambridge University Press, Cambridge, UK, 2012).
[15] J. Jiménez, Direct detection of linearized bursts in turbulence, Phys. Fluids **27**, 065102 (2015).
[16] R. J. Adrian, Hairpin vortex organization in wall turbulence, Phys. Fluids **19**, 041301 (2007).
[17] G. Kawahara, M. Uhlmann, and L. van Veen, The significance of simple invariant solutions in turbulent flows, Annu. Rev. Fluid Mech. **44**, 203 (2012).
[18] F. Waleffe, Three-Dimensional Coherent States in Plane Shear Flows, Phys. Rev. Lett. **81**, 4140 (1998).
[19] B. Hof, C. W. van Doorne, J. Westerweel, F. T. Nieuwstadt, H. Faisst, B. Eckhardt, H. Wedin, R. R. Kerswell, and F. Waleffe, Experimental observation of nonlinear traveling waves in turbulent pipe flow, Science **305**, 1594 (2004).
[20] J. F. Gibson, J. Halcrow, and P. Cvitanović, Visualizing the geometry of state space in plane Couette flow, J. Fluid Mech. **611**, 107 (2008).
[21] H. M. Blackburn, P. Hall, and S. J. Sherwin, Lower branch equilibria in Couette flow: The emergence of canonical states for arbitrary shear flows, J. Fluid Mech. **726**, R2 (2013).
[22] R. M. Clever and F. H. Busse, Tertiary and quaternary solutions for plane Couette flow, J. Fluid Mech. **344**, 137 (1997).
[23] Y. Duguet, P. Schlatter, D. S. Henningson, and B. Eckhardt, Self-Sustained Localized Structures in a Boundary-Layer Flow, Phys. Rev. Lett. **108**, 044501 (2012).
[24] H. Faisst and B. Eckhardt, Traveling Waves in Pipe Flow, Phys. Rev. Lett. **91**, 224502 (2003).
[25] J. F. Gibson, J. Halcrow, and P. Cvitanović, Equilibrium and traveling-wave solutions of plane Couette flow, J. Fluid Mech. **638**, 243 (2009).
[26] M. Nagata, Three-dimensional finite-amplitude solutions in plane Couette-flow bifurcation from infinity, J. Fluid Mech. **217**, 519 (1990).
[27] M. Nagata, Three-dimensional traveling-wave solutions in plane Couette flow, Phys. Rev. E **55**, 2023 (1997).
[28] T. M. Schneider, J. F. Gibson, and J. Burke, Snakes and Ladders: Localized Solutions of Plane Couette Flow, Phys. Rev. Lett. **104**, 104501 (2010).
[29] F. Waleffe, Exact coherent structures in channel flow, J. Fluid Mech. **435**, 93 (2001).
[30] F. Waleffe, Homotopy of exact coherent structures in plane shear flows, Phys. Fluids **15**, 1517 (2003).
[31] H. Wedin and R. R. Kerswell, Exact coherent structures in pipe flow: Travelling wave solutions, J. Fluid Mech. **508**, 333 (2004).

[32] F. Waleffe, On a self-sustaining process in shear flows, Phys. Fluids **9**, 883 (1997).
[33] T. Itano and S. Toh, The dynamics of bursting process in wall turbulence, J. Phys. Soc. Jpn. **70**, 703 (2001).
[34] G. Kawahara and S. Kida, Periodic motion embedded in plane Couette turbulence: Regeneration cycle and burst, J. Fluid Mech. **449**, 291 (2001).
[35] S. Toh and T. Itano, A periodic-like solution in channel flow, J. Fluid Mech. **481**, 67 (2003).
[36] L. van Veen and G. Kawahara, Homoclinic Tangle on the Edge of Shear Turbulence, Phys. Rev. Lett. **107**, 114501 (2011).
[37] D. Viswanath, Recurrent motions within plane Couette turbulence, J. Fluid Mech. **580**, 339 (2007).
[38] J. S. Park and M. D. Graham, Exact coherent states and connections to turbulent dynamics in minimal channel flow, J. Fluid Mech. **782**, 430 (2015).
[39] L. Xi and M. D. Graham, Active and Hibernating Turbulence in Minimal Channel Flow of Newtonian and Polymeric Fluids, Phys. Rev. Lett. **104**, 218301 (2010).
[40] L. Xi and M. D. Graham, Intermittent dynamics of turbulence hibernation in Newtonian and viscoelastic minimal channel flows, J. Fluid Mech. **693**, 433 (2012).
[41] M. D. Graham, Drag reduction and the dynamics of turbulence in simple and complex fluids, Phys. Fluids **26**, 101301 (2014).
[42] P. S. Virk, Drag reduction fundamentals, AIChE J. **21**, 625 (1975).
[43] G. Webber, R. Handler, and L. Sirovich, Karhunen-Loeve decomposition of minimal channel flow, Phys. Fluids **9**, 1054 (1997).
[44] A. Kushwaha, J. S. Park, and M. D. Graham, Temporal and spatial intermittencies within channel flow turbulence near transition, Phys. Rev. Fluids **2**, 024603 (2017).
[45] P. G. Drazin and W. H. Reid, *Hydrodynamic Stability*, Cambridge Monographs on Mechanics and Applied Mathematics (Cambridge University Press, Cambridge, UK, 1981).
[46] J. Wang, J. Gibson, and F. Waleffe, Lower Branch Coherent States in Shear Flows: Transition and Control, Phys. Rev. Lett. **98**, 204501 (2007).
[47] P. Hall and S. Sherwin, Streamwise vortices in shear flows: Harbingers of transition and the skeleton of coherent structures, J. Fluid Mech. **661**, 178 (2010).
[48] P. Hall and N. J. Horseman, The linear inviscid secondary instability of longitudinal vortex structures in boundary layers, J. Fluid Mech. **232**, 357 (1991).
[49] D. Viswanath, The critical layer in pipe flow at high Reynolds number, Philos. Trans. R. Soc. London A **367**, 561 (2009).
[50] K. Deguchi and P. Hall, Canonical exact coherent structures embedded in high Reynolds number flows, Philos. Trans. R. Soc. London A **372**, 20130352 (2014).
[51] J. F. Gibson and E. Brand, Spanwise-localized solutions of planar shear flows, J. Fluid Mech. **745**, 25 (2014).
[52] K. Deguchi and P. Hall, The high-Reynolds-number asymptotic development of nonlinear equilibrium states in plane Couette flow, J. Fluid Mech. **750**, 99 (2014).
[53] B. J. Mckeon and A. S. Sharma, A critical-layer framework for turbulent pipe flow, J. Fluid Mech. **658**, 336 (2010).
[54] A. S. Sharma and B. J. McKeon, On coherent structure in wall turbulence, J. Fluid Mech. **728**, 196 (2013).
[55] A. S. Sharma, R. Moarref, B. J. McKeon, J. S. Park, M. D. Graham, and A. P. Willis, Low-dimensional representations of exact coherent states of the Navier-Stokes equations from the resolvent model of wall turbulence, Phys. Rev. E **93**, 021102 (2016).
[56] J. F. Gibson, CHANNELFLOW: A spectral Navier-Stokes simulator in C++, Technical Report, University of New Hampshire, 2012, Channelflow.org.
[57] M. Nagata and K. Deguchi, Mirror-symmetric exact coherent states in plane Poiseuille flow, J. Fluid Mech. **735**, R4 (2013).
[58] S. A. Neelavara, Y. Duguet, and F. Lusseyran, State space analysis of minimal channel flow, Fluid Dynamics Res. **49**, 035511 (2017).
[59] S.-N. Wang, M. D. Graham, F. J. Hahn, and L. Xi, Time-series and extended Karhunen-Loève analysis of turbulent drag reduction in polymer solutions, AIChE J. **60**, 1460 (2014).

[60] L. Xi and M. D. Graham, Dynamics on the Laminar-Turbulent Boundary and the Origin of the Maximum Drag Reduction Asymptote, Phys. Rev. Lett. **108**, 028301 (2012).
[61] R. D. Whalley, J. S. Park, A. Kushwaha, D. J. C. Dennis, M. D. Graham, and R. J. Poole, Low-drag events in transitional wall-bounded turbulence, Phys. Rev. Fluids **2**, 034602 (2017).
[62] A. Shekar and M. D. Graham, Hairpin vortex exact coherent states in channel flow, arXiv:1709.02484v1.
[63] J. Guckenheimer and P. Holmes, *Nonlinear Oscillations, Dynamical Systems, and Bifurcations of Vector Fields* (Springer-Verlag, New York, 1983).
[64] F. Mellibovsky and B. Eckhardt, Takens–Bogdanov bifurcation of traveling-wave solutions in pipe flow, J. Fluid Mech. **670**, 96 (2011).
[65] K. Deguchi and P. Hall, On the instability of vortex-wave interaction states, J. Fluid Mech. **802**, 634 (2016).
[66] J. Zhou, R. J. Adrian, S. Balachandar, and T. M. Kendall, Mechanisms for generating coherent packets of hairpin vortices in channel flow, J. Fluid Mech. **387**, 353 (1999).
[67] J. Jeong, F. Hussain, W. Schoppa, and J. Kim, Coherent structures near the wall in a turbulent channel flow, J. Fluid Mech. **332**, 185 (1997).
[68] W. Schoppa and F. Hussain, Coherent structure generation in near-wall turbulence, J. Fluid Mech. **453**, 57 (2002).
[69] J. Kim and F. Hussain, Propagation velocity of perturbations in turbulent channel flow, Phys. Fluids **5**, 695 (1993).
[70] R. F. Blackwelder and J. H. Haritonidis, Scaling of the bursting frequency in turbulent boundary layers, J. Fluid Mech. **132**, 87 (1983).
[71] J. Kim and P. R. Spalart, Scaling of the bursting frequency in turbulent boundary layers at low Reynolds numbers, Phys. Fluids **30**, 3326 (1987).